Review

Structural characterization, thermal analysis, electric and dielectric properties of a novel organic-inorganic hybrid compound based on iron fluoride

Afef Moulahi[a], Oussama Guesmi[a], Mohammed S.M. Abdelbaky[b,*], Santiago García-Granda[b], Mohamed Dammak[a]

[a] Laboratoire de Chimie Inorganique, Faculté des Sciences de Sfax, Université de Sfax, 3000 Sfax, Tunisia
[b] Departamento de Química Física y Analítica, Universidad de Oviedo-CINN, 33006 Oviedo, Spain

ARTICLE INFO

ABSTRACT

A novel organic–inorganic hybrid compound based on iron fluoride, formulated as **(H$_2$Piper)$_4$ [(FeF$_6$)$_2$FeF$_5$(H$_2$O)(H$_2$O)$_4$]** (Piper = Piperazine), **C1**, has been synthesized through hydrothermal method and characterized by X-ray single-crystal diffraction, thermogravimetric analysis (TGA), differential scanning calorimetric (DSC) and dielectric measurements. Single-crystal X-ray study demonstrated that **C1** crystallizes in $P\ \bar{1}$ space group with lattice parameters: a = 12.5535(5) Å, b = 12.8715(4) Å, c = 22.2774(8) Å, α = 92.321(3)°, β = 95.957 (3)°, γ = 91.946(3)°, V = 3574.6 Å^3 and Z = 4. In the molecular arrangement, [FeF$_6$]$^{3-}$ and [FeF$_5$(H$_2$O)]$^{2-}$ anions are connected to [H$_2$Piper]$^{2+}$ cations and free water molecules through hydrogen bonds (O–H⋯F and N–H⋯F) generating 3D network. Thermal analysis (DSC and TG) of **C1** confirmed the presence of two phase transitions as well as the temperature of the decomposition of the hybrid material. The complex impedance of **C1** was investigated in the temperature range 410–530 K and in the frequency range 200–2.10^6 Hz. Additionally, an electrical equivalent circuit was reported to explain the impedance results. The variation of the dc and ac conductivity corroborated two phase transitions of the title compound. Furthermore, the frequency dependence of alternative current (ac) conductivity was interpreted in terms of Jonscher's law. The alternative current (ac) electrical conduction in **C1** material was accounted for in terms of two processes that can be assigned to the hopping transport mechanism (CBH and NSPT model). The temperature dependences of dielectric permittivity indicated a relaxation process and highlighted the good protonic conduction of this material.

Contents

* Corresponding author.
E-mail address: saidmohammed.uo@uniovi.es (M.S.M. Abdelbaky).

1. Introduction

Over the last decade, organic–inorganic hybrid compounds based on metal halide units have whetted the interest of researchers. This particularly refers to their ability to combine the interesting features of inorganic components (such as band gap tenability, mechanical and thermal stability, good electrical mobility, and magnetic or dielectric transitions) [1,2] and the properties of organic molecules (such as plastic mechanical property, structural diversity, ease of processing and efficient luminescence) as well as their ability to form of primordial weak interactions [3–14]. The numerous of types of recombination of these two matrices yield a competitive compound with an outstanding topological architecture that resulting in the enhancement of physical and chemical properties such as magnetic, luminescence, catalytic, electrical and ferroelectric characteristics [15–20].

Based on the nature of the interactions between the organic and inorganic parts, hybrid materials may belong to Class I hybrids, in which the different moieties are linked by weak interactions (such as van der Waals force or hydrogen bonds), or Class II hybrids, which exhibit the particularity of the central metal, where cation and the organic ligands are strongly linked by covalent or iono-covalent bonds [21].

In particular, iron fluoride hybrid systems in which fluoroferrate (II) or fluoroferrate(III) can be used to generate to fluorescent materials [22], stand for a very promising class of materials that may be invested in a wide range of technological applications deploying their electric and dielectric properties [23].

However, to the best of our knowledge, studies on the water – iron fluoride system have not been reported so far due to the hydrophobicity of fluorine based materials [24–26]. Our research work centers around the synthesis and structural characterization of hydrated iron fluoride materials ([Hdma](Fe$_2$(H$_2$O)$_4$F$_6$), [Hdma] (Fe$_2$(H$_2$O)$_4$F$_6$)·0.5H$_2$O, [Hdma](Fe$_2$F$_5$(H$_2$O)(Htaz)(taz)), Fe$_2$F$_5$(H$_2$O) (Htaz) (taz)(Hdma), [Fe$_3$F$_8$(H$_2$O)$_2$](Am$_2$TAZ)$_2$) [21,27,28], demonstrating that the existence of this unusual replacement of fluorine atom by H$_2$O molecule in anionic parts of hybrid compounds with piperazine, makes them worthwhile and valuable compounds that deserve to be characterized and enhanced in term of their structural and physical properties [29]. As part of our current research motivated by these previous reports, the attempt to use a different azo organic ligand yielded a novel compound, formulated as (H$_2$Piper)$_4$[(FeF$_6$)$_2$FeF$_5$(H$_2$O)(H$_2$O)$_4$]. Within this framework, we set forward the preparation, crystal characterization, scanning electron microscopy (SEM/EDX), thermal analysis (TGA and DSC) and dielectric properties of this novel 0-dimensional hybrid compound.

2. Experimental section

2.1. Synthesis of C1

The reaction mixture for the synthesis of novel class I hybrid fluoroferrate relies on two metal cations in fluorinated forms, namely FeF$_2$ and FeF$_3$, an aqueous solution of hydrofluoric acid 4% (prepared from 40% HF), a solvent such as water with a cyclic organic molecule (piperazine). The solvent volume was equal to 10 mL with a constant concentration [Fe^{2+}] + [Fe^{3+}] = 0.15 mol L^{-1} and an equimolar ratio n(Fe^{2+})/n(Fe^{3+}) = 1. Indeed, the mixture, involving 85 mg of FeF$_3$ (0.75 mmol), 70 mg of FeF$_2$ (1.5 mmol), 3.0 mL of HF (6.75 mmol) and 58.1 mg (piperazine) (6.75 mmol), yielded the compound (H$_2$Piper)$_4$[(FeF$_6$)$_2$FeF$_5$(H$_2$O)(H$_2$O)$_4$]. These materials were placed in a reactor in a way that they didn't fill 50% of the autoclave. Therefore, the investigating of this system FeF$_2$/FeF$_3$ – HF – Piperazine – H$_2$O by hydrothermal synthesis at 393 K, under autogenous pressure for 72 h, yielded the elaboration of a new phase that was white in color. After manipulation, this product was washed with water and dried at room temperature. This obtained product corresponded to a new hybrid fluoride with a chemical formula (H$_2$Piper)$_4$[(FeF$_6$)$_2$FeF$_5$(H$_2$O)(H$_2$O)$_4$].

2.2. Micrographs and X-ray microanalysis

Micrographs and X-ray microanalysis (SEM/EDX) were recorded using a JEOL-6610LV scanning electron microscope, which was operating at 30 kV, coupled with an X-Max Silicon Drift Detector for EDX analysis.

2.3. Determination of crystal structure

An optical microscope was used to select the single crystal. Data collection was performed on an Agilent Gemini CCD diffractometer using MoKα (λ = 0.71073 Å) radiation at room temperature. The WINGX package program was applied to solve the structure [30]. All the positions of the atoms (iron, fluorine, nitrogen, oxygen and carbon atoms) were specified by SHELXS-97 [31]. The refinement was carried out using full-matrix least square on all F^2 data by means of SHELXL-97 [31]. Thermal motion of all non-hydrogen atoms was refined using anisotropic method. All H atoms were, geometrically, placed riding on their parent atoms. The molecular graphics were performed through the DIAMOND program [32].

2.4. Thermal analysis

The thermogravimetric analysis of a 24.3154 mg of the sample was conducted using a Mettler-Toledo TGA/SDTA851ELF instrument, operating in oxygen flow at a heating rate of 10 K min^{-1}. This instrument was associated with a Pfeiffer Vacuum ThermoStar™ GSD301T mass spectrometer to determine the evacuated vapor of m/z 18 (H$_2$O), 20 (HF), 44 (CO$_2$) and 46 (NO$_2$).

2.5. Differential scanning calorimetry (DSC)

The differential scanning calorimetric (DSC) measurements were carried out with a NETZSCH STA 449F3T instrument. The powdered sample was heated from 400 K to 530 K, under a vacuum atmosphere controlled by MFC (Mass Flow Controllers).
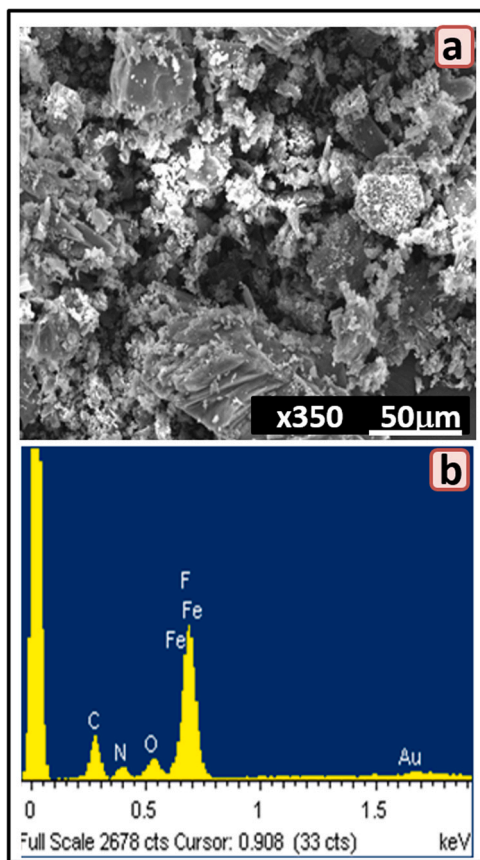
Fig. 1. (a): scanning electron microscopy image and (b): EDAX spectrum of C1.

Table 1
Crystal data and structure refinement forC1.

Chemical formula	$(H_2Piper)_4 \cdot [(FeF_6)_2 \cdot FeF_5 (H_2O) \cdot (H_2O)_4]$
M_r (g/mol)	933.25
Crystal system,	Triclinic
space group	P$\bar{1}$
Temperature (K)	293
a(Å)	12.8715 (4)
b (Å)	12.8715 (4)
c (Å)	22.2774 (8)
α (°)	92.321 (3)
β (°)	95.957 (3)
γ (°)	91.946 (3)
V (Å^3)	3574.6 (2)
Z	4
μ (mm^{-1})	1.33
Crystal size (mm)	0.17 × 0.13 × 0.09
R	0.095
wR	0.248
S	1.00

2.6. Electrical measurements

The electrical studies were performed in frequency ranges between 200 Hz and 2 MHz by means of electrode configurations. Indeed, the polycrystalline sample was pressed into 0.3 mm thick pellets with 4 mm diameter. These measurements were recorded in the temperature range from 410 K to 530 K using a TEGAM 3550 ALF automatic bridge monitored by a microcomputer.

3. Results and discussion

3.1. Microstructural studies

SEM images indicated the plate-like single-crystals and microcrystalline powder of the title compound. EDX analysis confirmed that all non-hydrogen atoms are present: Fe, F, O, N and C (Fig. 1).

3.2. Structural analysis

The X-ray single-crystal analysis of **C1** revealed that its diffractable crystals belong to the triclinic system P $\bar{1}$ with the unit cell parameters $a = 12.5535(5)$ Å, $b = 12.8715(4)$ Å, $c = 22.2774(8)$ Å, $\alpha = 92.321(3)°$, $\beta = 95.957(3)°$, $\gamma = 91.946(3)°$, V = 3574.6(2) Å^3 and Z = 4. A summary of the crystallographic data and structure refinement parameters is displayed in Table 1, whereas the selected bond distances and angles are exhibited in Table 2. The structure of **C1** is built up of two types of isolated octahedral, {FeF$_6$} and {FeF$_5$(H$_2$O)}, separated by [H$_2$Piper]$^{2+}$ cations and water molecules. Examining this structure unveiled that cationic part occupies special positions

but the anionic components located in general positions (Fig. 2). It also revealed that there is an alternation of organic-inorganic layers running parallel to the c axis (Fig. 3). Within the crystal, Iron atom is coordinated by six fluorine atoms forming {FeF$_6$} octahedron. However, the {FeF$_5$(H$_2$O)} octahedron is constructed by five fluorine atoms and one water molecule coordinated to the iron atom. The Fe–F bond length varies between 1.853(4) Å and 1.977(4) Å, whereas the F–Fe–F and F–Fe–O angles lie in the range between 85.55(17)° and 177.6(2)°. The lower values interaction of iron-fluoride involves that the oxidation state is (+III) for iron atoms [33]. All distances C–C, C–N and N–N go in a good agreement with literature [34]. The measurement of the distortion indices (DI) of the iron octahedron environment in this new hybrid compound indicated the presence of six different types of octahedron: four of FeF$_6$ octahedron and two of FeF$_5$(H$_2$O) octahedron. These values were calculated using the distortion equations indices (DI) of Baur [35]:

$$DI(Fe - X) = \frac{\sum_{i=1}^{6} |d_i - d_m|}{6d_m}$$

$$DI(X - Fe - X) = \frac{\sum_{i=1}^{12} |a_i - a_m|}{6a_m}$$

where: 'X' is fluorine or oxygen atom, 'd' is the Fe–X distance, 'a' is the X–Fe–X angle, and 'm' is the average value.

Table 3 illustrates DI value of each type of octahedron. These results demonstrate that the coordination geometry of iron for FeF$_5$(H$_2$O) octahedron is more slightly distorted than FeF$_6$ octahedron from the regular form of octahedron. This is assigned basically to the existence of H$_2$O in the coordination sphere of iron.

As shown in Fig. 3 the structure is stabilized by intermolecular hydrogen-bonding interactions forming a pseudo 3D network. The cohesion between both octahedrons FeF$_6$ and FeF$_5$(H$_2$O) is ensured by a hydrogen bond of the type O–H⋯F, which refers to the substitution of the atom of fluorine by water molecule. This hydrogen bond ranges from 2.553(7) Å to 2.629(6) Å, leading to a chain parallel to the b axis. The N–H⋯F hydrogen bonds are formed between the hydrogen atoms of the organic entities and the fluorine atoms of inorganic anions. The free water molecules and inorganic species, [FeF$_6$]$^{3-}$ and [FeF$_5$(H$_2$O)]$^{2-}$, are associated by hydrogen bonds of the nature O–H⋯F. The strength of hydrogen bonds is accounted for in terms of the d(D⋯A) distance using the classification of Jeffrey [36]. All hydrogen bonds are considered to be moderate, 2.553(7) Å < d (A⋯D) < 3.142(8) Å (Table 4).

Table 2
Selected bond distances [Å] and angles [°] in C1.

Distances (Å)					
Fe1—F13	1.892 (4)	Fe5—F56	1.907 (4)	N15—C32	1.490 (9)
Fe1—F11	1.907 (4)	Fe5—F53	1.923 (4)	N15—C29	1.491 (8)
Fe1—F16	1.925 (4)	Fe5—F52	1.950 (4)	N10—C19	1.461 (9)
Fe1—F14	1.927 (4)	Fe5—F51	1.955 (4)	N10—C20i	1.495 (9)
Fe1—F15	1.934 (4)	Fe5—F54	1.955 (4)	N3—C6ii	1.472 (9)
Fe1—F12	1.977 (4)	Fe6—F65	1.894 (4)	N3—C5	1.481 (9)
Fe2—F23	1.853 (4)	Fe6—F62	1.918 (4)	N11—C21	1.460 (10)
Fe2—F21	1.910 (4)	Fe6—F66	1.919 (4)	N11—C22iii	1.480 (9)
Fe2—F22	1.913 (4)	Fe6—F63	1.926 (4)	N5—C9	1.467 (9)
Fe2—F25	1.918 (4)	Fe6—F61	1.948 (4)	N5—C10	1.497 (10)
Fe2—F24	1.942 (4)	Fe6—F64	1.964 (4)	N14—C27	1.488 (9)
Fe2—O2	2.155 (5)	Fe5—F56	1.907 (4)	N14—C26	1.497 (10)
Fe3—F36	1.919 (4)	N6—C11	1.482 (9)	N13—C25	1.475 (9)
Fe3—F35	1.924 (4)	N6—C12	1.490 (8)	N13—C28	1.494 (10)
Fe3—F31	1.941 (4)	N4—C8	1.484 (8)	N12—C23	1.442 (10)
Fe3—F33	1.942 (4)	N4—C7	1.493 (8)	N12—C24	1.492 (11)
Fe3—F32	1.953 (4)	N9—C17	1.484 (9)	C6—N3ii	1.472 (9)
Fe4—F45	1.895 (4)	N9—C18	1.500 (9)	C16—N8	1.351 (13)
Fe4—F42	1.907 (4)	N2—C2	1.471 (9)	C13—N7	1.365 (12)
Fe4—F41	1.916 (4)	N2—C3	1.481 (9)	C22—N11iii	1.480 (9)
Fe4—F44	1.929 (4)	N1—C1	1.476 (8)	C14—N7	1.321 (12)
Fe4—F43	1.942 (4)	N1—C4	1.500 (9)	C15—N8	1.341 (12)
Fe4—O4	2.130 (4)	N16—C31	1.484 (9)		
Fe5—F55	1.899 (4)	N16—C30	1.497 (9)		

Angles (°)				
F13—Fe1—F11	92.5 (2)	F53—Fe5—F51	91.61 (17)	
F13—Fe1—F16	171.0 (2)	F52—Fe5—F51	88.41 (17)	
F11—Fe1—F16	90.3 (2)	F55—Fe5—F54	176.78 (19)	
F13—Fe1—F14	91.0 (2)	F56—Fe5—F54	88.33 (19)	
F11—Fe1—F14	175.1 (2)	F53—Fe5—F54	89.23 (17)	
F16—Fe1—F14	86.76 (19)	F52—Fe5—F54	88.99 (17)	
F13—Fe1—F15	91.9 (2)	F51—Fe5—F54	86.35 (17)	
F11—Fe1—F15	88.4 (2)	F65—Fe6—F62	177.0 (2)	
F16—Fe1—F15	96.72 (18)	F65—Fe6—F66	92.8 (2)	
F14—Fe1—F15	88.11 (18)	F62—Fe6—F66	88.42 (19)	
F13—Fe1—F12	85.89 (19)	F65—Fe6—F63	91.1 (2)	
F11—Fe1—F12	89.7 (2)	F62—Fe6—F63	87.8 (2)	
F16—Fe1—F12	85.55 (17)	F66—Fe6—F63	175.7 (2)	
F14—Fe1—F12	93.92 (18)	F65—Fe6—F61	88.4 (2)	
F15—Fe1—F12	177.05 (16)	F62—Fe6—F61	94.32 (19)	
F23—Fe2—F21	91.6 (2)	F66—Fe6—F61	90.75 (18)	
F23—Fe2—F22	94.9 (2)	F63—Fe6—F61	87.45 (19)	
F21—Fe2—F22	89.30 (18)	F65—Fe6—F64	88.1 (2)	
F23—Fe2—F25	93.2 (2)	F62—Fe6—F64	89.10 (18)	
F21—Fe2—F25	91.06 (18)	F66—Fe6—F64	90.89 (19)	
F22—Fe2—F25	171.83 (19)	F63—Fe6—F64	91.14 (19)	
F23—Fe2—F24	95.7 (2)	F61—Fe6—F64	176.25 (18)	
F21—Fe2—F24	172.5 (2)	C11—N6—C12	112.5 (6)	
F22—Fe2—F24	91.40 (18)	C8—N4—C7	110.4 (6)	
F25—Fe2—F24	87.20 (17)	C17—N9—C18	111.5 (6)	
F23—Fe2—O2	177.5 (2)	C2—N2—C3	112.2 (6)	
F21—Fe2—O2	86.12 (18)	C1—N1—C4	110.3 (6)	
F22—Fe2—O2	86.00 (19)	C31—N16—C30	111.4 (6)	
F25—Fe2—O2	85.88 (19)	C32—N15—C29	111.4 (6)	
F24—Fe2—O2	86.50 (18)	C19—N10—C20i	110.6 (6)	
F34—Fe3—F36	94.2 (2)	C6ii—N3—C5	109.9 (6)	
F34—Fe3—F35	89.52 (18)	C21—N11—C22iii	110.5 (6)	
F36—Fe3—F35	89.39 (19)	C9—N5—C10	110.8 (6)	
F34—Fe3—F31	177.5 (2)	C27—N14—C26	110.5 (6)	
F36—Fe3—F31	88.2 (2)	C25—N13—C28	113.2 (6)	
F35—Fe3—F31	89.91 (18)	C23—N12—C24	111.2 (7)	
F34—Fe3—F33	90.76 (18)	N2—C2—C1	110.0 (6)	
F36—Fe3—F33	174.50 (19)	N6—C11—C12iv	110.4 (5)	
F35—Fe3—F33	93.00 (18)	N4—C8—C7v	109.7 (6)	
F31—Fe3—F33	86.84 (18)	N6—C12—C11iv	110.2 (6)	
F34—Fe3—F32	90.90 (18)	N9—C18—C17vi	110.2 (6)	
F36—Fe3—F32	87.89 (19)	N2—C3—C4	110.6 (6)	
F35—Fe3—F32	177.27 (18)	N14—C26—C25	110.9 (7)	
F31—Fe3—F32	89.78 (19)	N13—C25—C26	109.7 (6)	
F33—Fe3—F32	89.69 (17)	N4—C7—C8v	110.3 (6)	
F45—Fe4—F42	94.88(18)	N1—C1—C2	110.3 (6)	
F45—Fe4—F41	87.04(18)	N13—C28—C27	109.3 (6)	
F42—Fe4—F41	93.41(18)	N16—C30—C29	109.8 (6)	
F45—Fe4—F44	92.51(18)	N16—C31—C32	111.1 (6)	
F42—Fe4—F44	94.01(18)	N15—C32—C31	111.0 (6)	

Table 2 (*continued*)

F41—Fe4—F44	172.58(17)	N3—C5—C6	110.2 (6)
F45—Fe4—F43	174.70(18)	N1—C4—C3	109.9 (6)
F42—Fe4—F43	89.52 (18)	N3ii—C6—C5	109.3 (6)
F41—Fe4—F43	89.75 (18)	N10i—C20—C19	110.5 (6)
F44—Fe4—F43	90.12 (18)	N10—C19—C20	110.3 (6)
F45—Fe4—O4	87.49 (19)	N11—C21—C22	111.4 (7)
F42—Fe4—O4	177.6 (2)	N15—C29—C30	110.3 (6)
F41—Fe4—O4	86.90 (18)	N7—C13—C16	114.5 (8)
F44—Fe4—O4	85.68 (18)	N8—C16—C13	111.4 (8)
F43—Fe4—O4	88.13 (19)	N11iii—C22—C21	110.6 (6)
F55—Fe5—F56	94.20 (19)	N14—C27—C28	111.3 (6)
F55—Fe5—F53	88.75 (17)	N5—C9—C10vii	110.4 (6)
F56—Fe5—F53	90.70 (19)	N5—C10—C9vii	109.5 (6)
F55—Fe5—F52	93.03 (18)	N7—C14—C15	114.4 (8)
F56—Fe5—F52	89.11 (18)	N8—C15—C14	112.6 (8)
F53—Fe5—F52	178.22(16)	N12—C23—C24viii	111.3 (7)
F55—Fe5—F51	91.21 (17)	C23viii—C24—N12	109.6 (7)
F56—Fe5—F51	174.16(18)	C15—N8—C16	132.4 (9)
C14—N7—C13	130.6 (9)		

Symmetry codes: (i) −x + 1, −y + 2, −z + 2; (ii) −x + 1, −y + 1, −z + 1; (iii) −x + 1, −y + 2, −z + 1; (iv) x, y + 1, z; (v) x − 1, y − 1, z; (vi) x + 1, y, z; (vii) x, y − 1, z; (viii) −x, −y + 1, −z + 1.
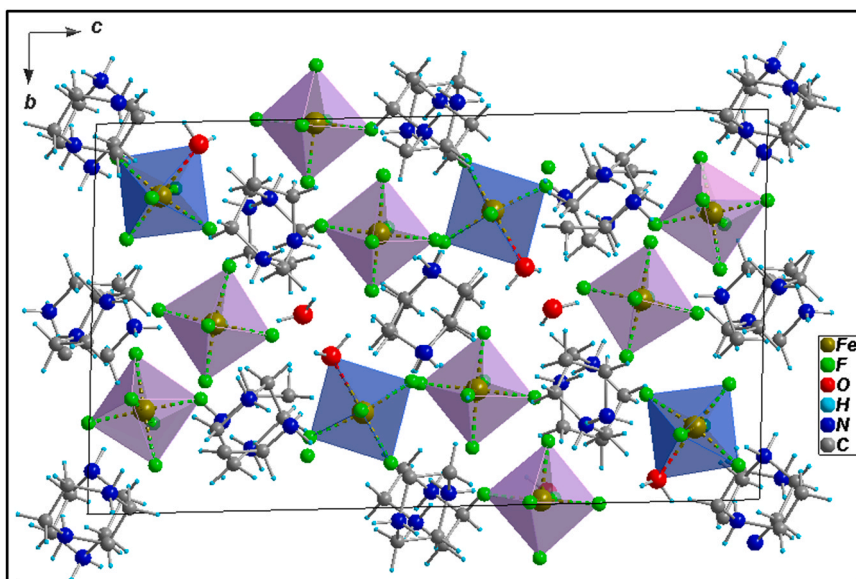

Fig. 2. View of C1 along a axis.

3.3. Thermal behavior

The thermal stability of **C1** was investigated. TG/DTG curves and the mass spectrometry analysis are depicted in Fig. 4 and 5, while DSC traces are plotted in Fig. 6. TG/ DTG curves of **C1** reveal a total experimental weight loss of 73.1% (calc.: 73.05%) that takes place in four steps during the heating process, from room temperature up to 1196 K. The first weight loss appeared in the TG curve between 335 K and 400 K with a mass loss of ca 4.4% (cal.: 4.30%) corresponding to the loss of 1 mol of water and 2 mol of hydrofluoric acid (HF). The second weight loss (exp.: 3.3%, cal.: 3.65%) demonstrated by TG curve between 405 K and 447 K, can be attributed to the loss of 1.5 mol of H_2O and 1 mol of HF. The third weight loss of sample (exp = 8.3%; cal = 8.32%) occurring between 447 K and 500 K, can be assigned to the loss of 1.5 mol of H_2O and 4 mol of HF. All these results are confirmed by mass spectroscopy *m/z* 18 and *m/z* 20 analyses [26,33]. The final achievement of the three FeF$_3$ molecules results obtained after the decomposition of the organic molecule is associated with the release of CO_2 and NO_2, the elimination of HF molecules and the total dehydration of the compound. This is shown in the corresponding curves *m/z* 18, 20, 44 and 46 [28].

The DSC curve, in the 400–530 K temperature range, presents two endothermic peaks at 433 K and 462 K that may be attributed to order-disorder phase transition. These results display interesting electrical properties.

3.4. Electrical properties

3.4.1. Impedance analysis and equivalent circuit

The electrical properties of **C1** were explored by complex impedance spectroscopy in the frequency range [200 Hz-2 MHz] between 410 K and 530 K giving us information about the reactive (imaginary part Z″) and resistive (real part Z′) components in the material. Fig. 7 shows the Nyquist plots taken at different temperatures and depict the variation between the imaginary part of complex impedance (Z″) versus the real part of complex impedance (Z′) of (**C1**) and exhibit some dispersion instead of being a semicircle centered on the real axis, which indicates a Cole-Cole empirical behavior. Therefore, the increase of the temperature is
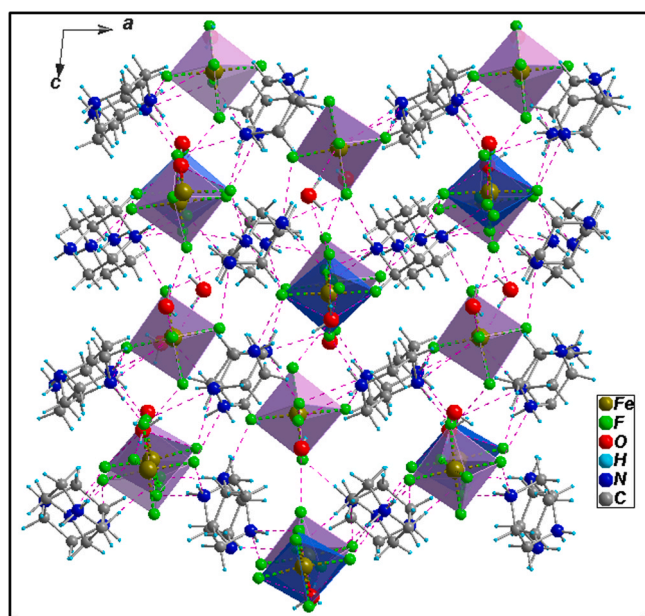
Fig. 3. Projection of the crystal packing of C1 in *ac*-plane. The O–H···F and N–H···F interactions between structural components are presented by pink dashed lines.

Table 4
Hydrogen bonds in C1.

D—H···A	D···A	D—H···A	D···A
O2—H22···F54	2.629 (6)	N12—H12A···F64	2.753 (8)
O2—H21···F63	2.605 (6)	N12—H12B···F21	2.633 (8)
O4—H42···F31	2.613 (6)	O7—H72···F24	2.795 (8)
O4—H41···F11	2.553 (7)	O10—H12···F33^i	2.704 (6)
O10—H11···F65	2.639 (7)	N6—H6A···F53^{ii}	2.734 (6)
N6—H6B···F42	2.750 (7)	N6—H6A···F55^{ii}	2.884 (7)
N4—H4A···F14	2.673 (7)	N4—H4B···F55^{iii}	2.757 (7)
N9—H9B···F35	2.672 (7)	N4—H4B···F42^{iv}	3.040 (7)
N2—H2A···F24	2.663 (7)	N9—H9A···F66^v	2.731 (7)
N2—H2B···F52	2.701 (7)	O12—H9BA···F41^{ii}	2.682 (7)
N2—H2B···F51	2.869 (7)	N16—H16A···F33^{vi}	2.698 (7)
O12—HD···F51	2.691 (6)	N16—H16B···F12^{vi}	2.672 (6)
N1—H1B···F16	2.576 (7)	N16—H16B···F16^{vi}	2.966 (7)
N1—H1A···F32	2.690 (7)	N10—H10A···F61^i	2.750 (7)
N15—H15A···F51	2.701 (7)	N10—H10A···F66^i	3.112 (7)
N15—H15B···F25	2.609 (6)	O5—H52···F56^{iii}	2.674 (7)
N15—H15B···F24	3.122 (7)	N3—H3A···F45^{ii}	2.799 (7)
N10—H10B···F34	2.641 (7)	N3—H3A···F41^{ii}	2.952 (7)
O5—H51···F13	2.571 (7)	N11—H11B···F61^i	2.858 (8)
N3—H3B···F15	2.661 (7)	N11—H11B···F63^i	3.102 (7)
N11—H11A···F22	2.655 (7)	O9—H92···F14^{vii}	2.869 (7)
O9—H91···F44	2.793 (7)	N5—H5B···F41^{viii}	2.817 (8)
N5—H5A···F12	2.689 (7)	N5—H5B···F43^{viii}	2.931 (8)
N14—H14B···F62	2.668 (8)	N13—H13B···F32^{iv}	2.724 (7)
N14—H14A···F52	2.708 (7)	N13—H13B···F36^{iv}	3.041 (8)
N14—H14A···F56	3.142 (8)	N13—H13A···F44^{iv}	2.699 (7)
N12—H12A···F64	2.753 (8)	O7—H71···F66^{vii}	3.054 (9)

Symmetry codes: (i) $-x+1$, $-y+2$, $-z+2$; (ii) $-x+1$, $-y+1$, $-z+1$; (iii) $-x+1$, $-y+2$, $-z+1$; (iv) x, $y+1$, z; (v) $x-1$, $y-1$, z; (vi) $x+1$, y, z; (vii) x, $y-1$, z; (viii) $-x$, $-y+1$, $-z+1$.

accompanied by a decrease of the radius of semicircles and then a decrease in resistance. These observations imply that the conductivity is thermally activated [37].

The Zview software was used to fit the measured impedance data along with a typical equivalent circuit composed of two elements connected in parallel: a resistance R and a fractal capacity CPE (Fig. 8). In this case, the impedance of the capacity of fractal interface CPE is determined by the following expression:

$$Z_{(CPE)} = \frac{1}{Q\,(i\omega)^\alpha}$$

where, Q is the value of capacitance of the CPE element and α is the fractal exponent.

The previous equation demonstrates that if: α = 1, then, $Z_{(CPE)} = 1/iQ\omega$ and the CPE involves a pure capacitance. However, if: α = 0, then, $Z_{(CPE)} = 1/Q$ and the CPE involves a pure resistance. In this case, α = 0.24 at different temperatures (Fig. 9).

The real (Z′) and imaginary (Z″) components of the impedance were calculated in terms of the following equations:

$$Z' = \frac{R\left(RA_0\omega^\alpha\cos\left(\frac{\alpha\pi}{2}\right)+1\right)}{\left[\left(1+RA_0\omega^\alpha\cos\left(\frac{\alpha\pi}{2}\right)\right)^2+\left(RA_0\omega^\alpha\sin\left(\frac{\alpha\pi}{2}\right)\right)^2\right]}$$
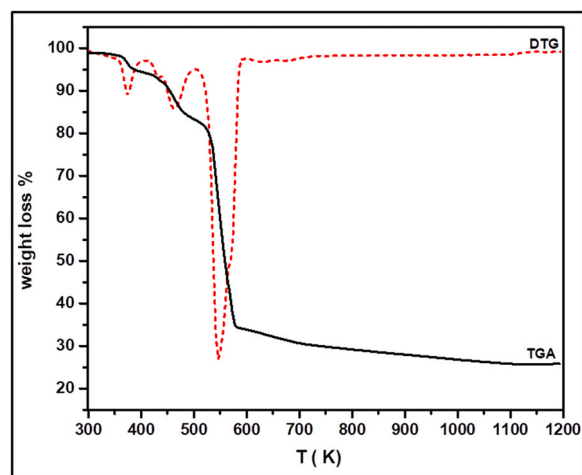
$$Z'' = \frac{\left(R^2A_0\omega^\alpha\sin\left(\frac{\alpha\pi}{2}\right)\right)}{\left[\left(1+RA_0\omega^\alpha\cos\left(\frac{\alpha\pi}{2}\right)\right)^2+\left(RA_0\omega^\alpha\sin\left(\frac{\alpha\pi}{2}\right)\right)^2\right]}$$

Fig. 4. TG and DTG curves of C1.

Fig. 10 depicts Z′ and Z″ versus frequencies together with fits to the equivalent circuit portrayed in Fig. 8. At 480 K temperature, a good agreement between the experimental and the theoretical curve of the real and imaginary impedance is recorded. All fitted curves at each temperature indicate the good conformity of the calculated lines with the experimental data, denoting that the proposed
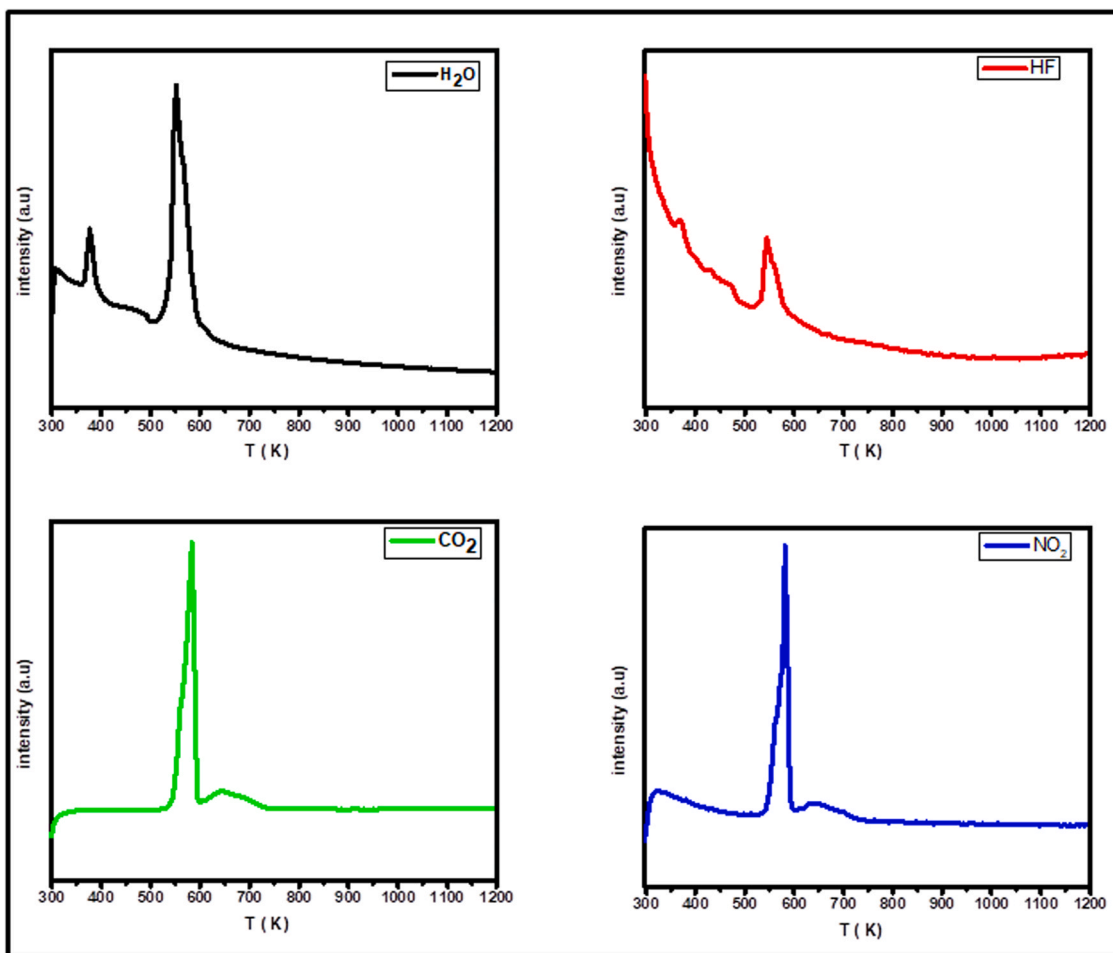
Table 3
The distortion indices of iron environment in C1.

FeF$_6$ octahedron			FeF$_5$ (H$_2$O) octahedron		
	DI (Fe–X)	DI (X –Fe– X)		DI (Fe–X)	DI (X –Fe– X)
Fe(1)F$_6$	0,0099	0,0317	**Fe(2)F$_5$(H$_2$O)**	0,0353	0,0342
Fe(3)F$_6$	0,0080	0,0164	**Fe(4)F$_5$(H$_2$O)**	0,0302	0,0235
Fe(5)F$_6$	0,0113	0,0200			
Fe(6)F$_6$	0,0096	0,0201			

Fig. 5. *m/z* 18 (H2O), 20 (HF), 44 (CO2) and 46 (NO2) MS signals of evacuated vapours, for C1.
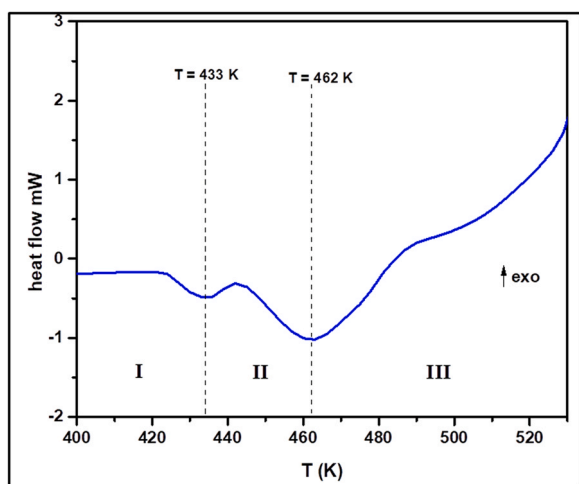

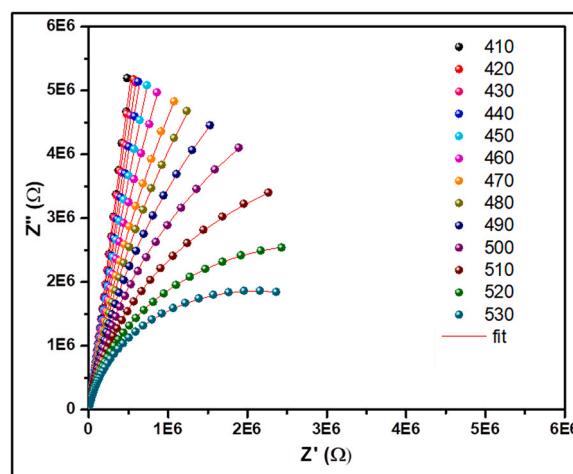**Fig. 6.** Differential Scanning Calorimetry of C1.

Fig. 7. Nyquist plots (Z″ vs. Z′) at different temperatures for C1compound.

equivalent circuit describes quite well the electrical properties of the compound.

The dc conductivity was computed as follows:

$$\sigma_{dc} = \frac{e}{(R*S)}$$

where, R is the resistance obtained by data fit of the impedance spectra, S is the area of sample and e is the sample thickness.

The variation of specific conductivity (Ln (σ_{dc}T)) versus 1000/T is illustrated in Fig. 11.

As it is noticed, this curve is indicative of a rise in the conductivity of the material with an increase in temperature. Such behavior suggests that the conduction in the compound is a thermally activated transport mechanism governed by the Arrhenius law: σ_{dc}T = σ_0 exp (- Ea/kT). Three regions (I), (II) and (III) were identified
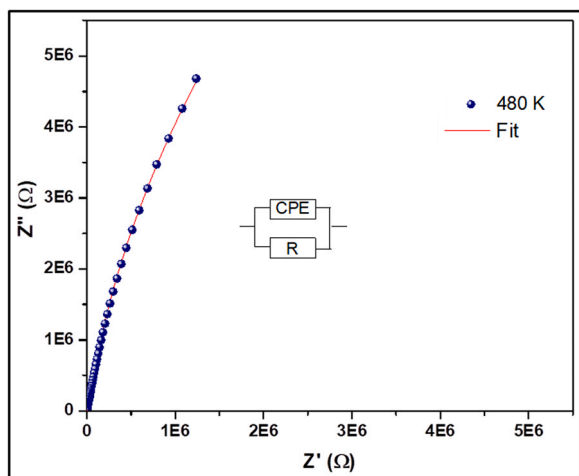
Fig. 8. Simulated Nyquist plots with equivalent circuit elements for C1 compound at 480 K.
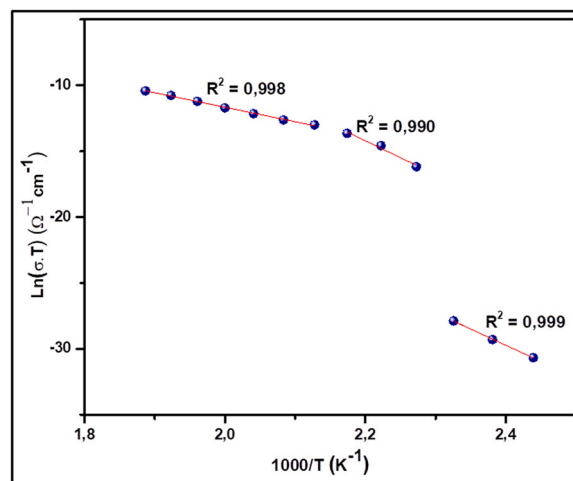

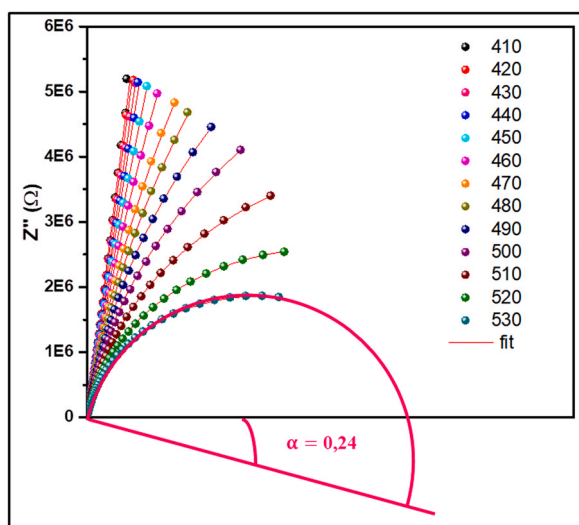**Fig. 11.** Variation of the Ln (σ$_{dc}$T)) versus 1000/T of the title compound.

by the change of slope at $T_1 = 440$ K and $T_2 = 470$ K, confirming the conduction phase transition in this material [38]. Furthermore, the activation energy which was calculated by the linear fit of the curve conductivity identified through Fig. 11 in regions (I), (II) and (III), are $E_{aI} = 2.12$ eV, $E_{aII} = 2.21$ eV and $E_{aIII} = 0.95$ eV, respectively.

The conductivity plot corroborates that this material displays a super-protonic conduction that may be assigned to the breaking of O–H···F and N–H···F hydrogen bonds after dehydration and may also be attributed to a drastic rebuilding of the crystal structure accompanying a chemical transformation [16,38].

3.4.2. Ac electrical conductivity

The electric conductivity σ$_{ac}$ is a key approach in terms of displaying information about the electrical dynamic including conductivity, capacitance and loss factor in the sample. It is also useful to identify the nature of the conduction.

The ac conductivity results from impedance complex data specified according to the following equation:

$$\sigma_{ac} = \left(\frac{e}{s}\right)\left[\frac{Z'}{(Z^2 + Z'^2)}\right]$$

The variation of the ac conductivity according to the frequency at different temperatures is illustrated in Fig. 12. It is noteworthy that the conductivity (σ$_{ac}$) curves for the studied sample reveal two different regions: at low frequency it is constant but it exhibits

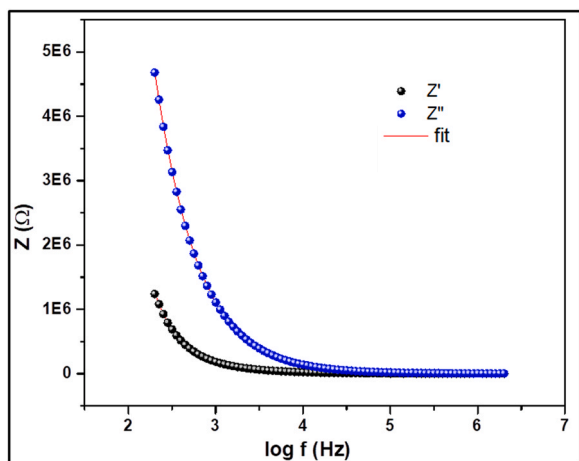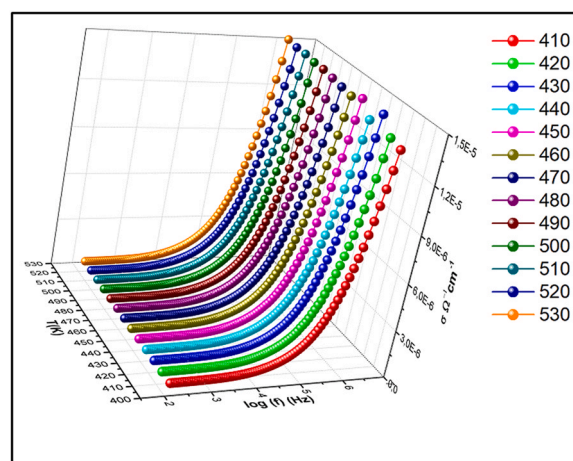**Fig. 9.** Cole–Cole plot and its inset representing the determination of α.

Fig. 10. The variation of the real and the imaginary parts of the impedance. (Z′ and Z″) according the frequency at 480 K.

Fig. 12. The variation of the ac conductivity according to the frequency at different temperatures.
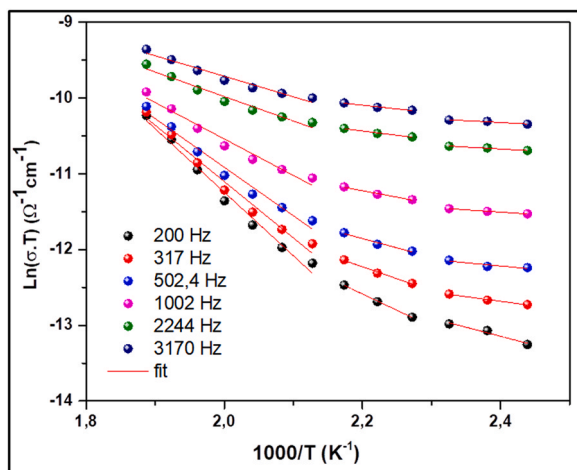
Fig. 13. Variation of the (Ln (σ_{ac}T)) versus 1000/T of the title compound.

Fig. 14. Frequency dependence of activation energy at different regions of the title compound.

dispersion at high frequency. Therefore, the rise in frequency makes better the jumping frequency of charge carriers, generating a rise of the conduction process and then an increase of the conductivity. Moreover, this feature indicates the presence of a thermally activated process triggered by an increase pertaining to the energy of the charge carriers. At lower frequencies, the applied electric field forces the charge carriers to move over large distances [37]. Hence, the main movements of the charge carriers are decrease with the rise of frequency [39–41].

The Fig. 13 summarizes the temperature dependence of ac conductivity for the title compound at different frequencies in the form (Ln (σ_{ac}T)) versus 1000/T, which clearly reveals three distinct regions presumably corresponding to different conduction mechanisms. Furthermore, the experimental values of ac conductivity are fitted to the Arrhenius-type behavior expressed by the following equation [38]:

$$\sigma_{ac} = A \exp\left(\frac{E_a}{k_B T}\right)$$

where, A represents the pre-exponential factor, Ea stands for the activation energy, k_B corresponds to the Boltzmann's constant and T refers to the absolute temperature.

This variation is described by the Arrhenius relation and characterizes the three regions which are confirmed by the change of the curve slope at $T_1 = 440$ K and $T_2 = 470$ K.

As for the frequency variations of the obtained activation energy Ea, they are displayed in Fig. 14. Therefore, it is evident that the activation energy decreases with the increase in frequency. This result proves that the applied field frequency ameliorates the electronic jumps between the localized states.

3.4.3. Theory investigation of the conduction mechanism

Fig. 15 depicts the frequency-dependent conductivity data which are fitted in the Jonscher's universal power law [42] indicated in terms of:

$$\sigma_{ac}(\omega) = \sigma_{dc} + A\omega^s$$

where σ_{dc} is the dc conductivity, ω is the angular frequency of measurement and A and s are fitting parameters, that are mainly temperature dependent. The exponent (s) with values in the range 0 < s < 1, represents the degree of interaction between mobile ions with the environments surrounding them [43,44].

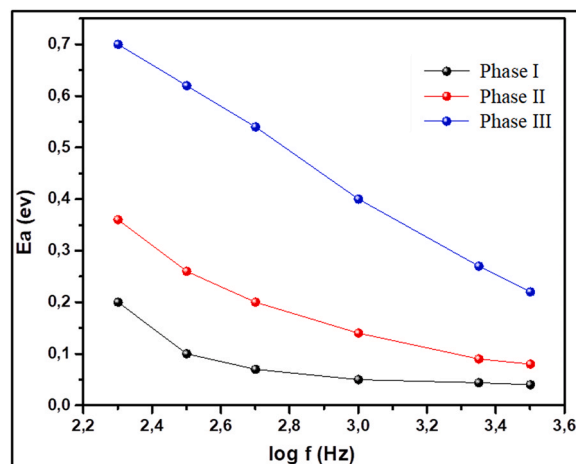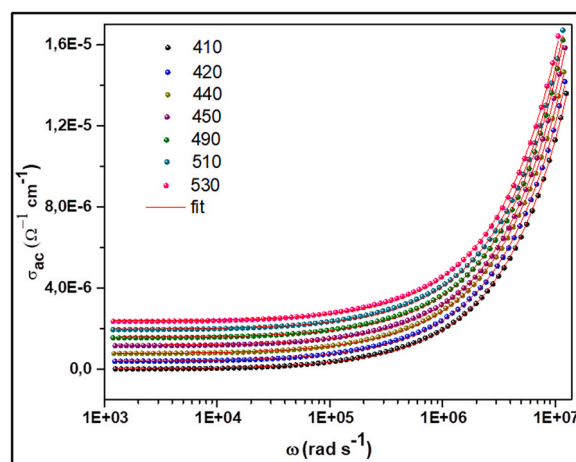**Fig. 15.** The frequency-dependent conductivity data which are fitted in the Jonscher's universal power law.

In order to find the predominant conduction mechanism of the ac conductivity of the sample, the convenient mode for the conduction mechanism is introduced taking into account the several theoretical models which associate the conduction mechanism of ac conductivity with s(T) behavior [45] (Fig. 16).

In literature, four models have been considered relying on two distinct processes, which correspond, classical hopping over a barrier and quantum-mechanical tunneling, or some certain variations or combinations of the two processes. It has been differently supposed that electrons (or polarons) or atoms are the responsible carriers [46].

These models are:

– The quantum mechanical tunneling (QMT) model: where the exponent (s) is almost equal to 0.8 and temperature independent or increases slightly with temperature [47,48].
– The correlated barrier hopping (CBH) model: where the exponent (s) decreases with the rise in temperature [49].
– The overlapping large-polaron tunneling (OLPT) model: where the exponent (s) depends on both frequency and temperature and decreases with an increase in temperature to a minimum value and then rises as temperature increases [46].
– The non-overlapping small polaron tunneling (NSPT) model: where the exponent (s) increases with temperature increase [50].
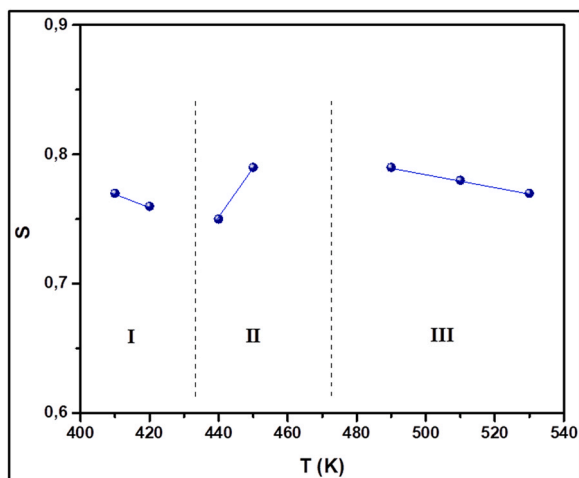
Fig. 16. Temperature dependence of the exponent s.

Fig. 17. The temperature dependence of ε_r' for C1.

Fig. 16 illustrates the variation of the exponent (s) as a function of temperature. These values proved to be conversely varied. Departing from this figure, it is obvious that two fundamental mechanisms are observed: First, the values of (s) decrease with the increasing temperature in phase (I) and (III), suggesting that the Correlated Barrier Hopping (CBH) model is the suitable model for these regions, where the charge carrier hops between the sites over the potential barrier separates them [49]. Second, the values of (s) increase with temperature rise in region (II) indicating that the non-overlapping small polaron tunneling (NSPT) model is the most appropriate one to characterize the electrical conduction mechanism in this region, indicating in turn the activated behavior of polarons, which is independent of interstice separation [51].

3.5. Dielectric studies

Dielectric properties of materials are molecular properties which are fundamental in all the materials that are capable of impending electron movement resulting in polarization within the material on exposure to an external electric field. As a matter of fact, the existence of inertia to the charge moment entails a relaxation in polarization [48]. Dielectric relaxation is an important approach to get reliable information about mechanisms of conduction as well as the origin of the dielectric losses, and to characterize the phase transition detected in the DSC curve. The dielectric relaxation is defined by a non-Debye model which can be expressed as:

$$\varepsilon^* = \varepsilon' + i\varepsilon''$$

Real and imaginary parts of the electric permittivity were calculated according to the following relations:

$$\varepsilon' = \frac{-Z''}{\omega C_0 (Z'^2 + Z''^2)}$$

$$\varepsilon'' = \frac{-Z'}{\omega C_0 (Z'^2 + Z''^2)}$$

The temperature dependence of (ε') and (ε'') (real and imaginary parts) of the electric permittivity for the title compound are illustrated in Figs. 17 and 18. It's clear that, at T < 430 K, the variation of ε' and ε'' with temperature is nearly constant. This can be explained by the restricted reorientational motions of the proton, which are unable to orient themselves with respect to the direction of the applied electric field. Yet, they display a weak contribution to polarization [38].
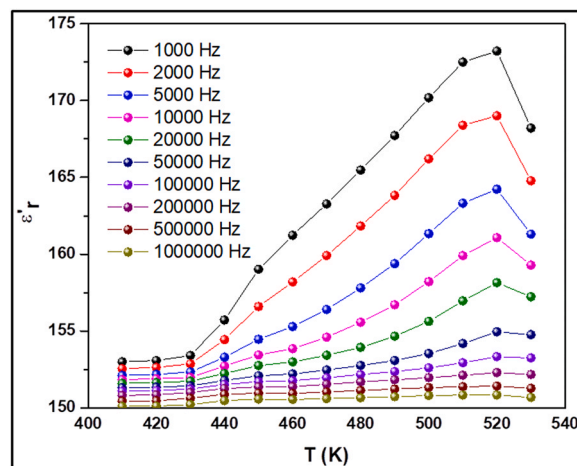
Over this temperature, where T > 430 K, the reorientational dynamics of protons is activated. The cation has enough excitation thermal energy allowing it abides by the change in the external electric field more easily. This in turn improves its contribution to the polarization leading to an increase in dielectric behavior.

A large peak is observed at low frequencies in these spectra. According to the DSC curve, this peak is the maximum point of two peaks: The first peak of low intensity at around T = 450 K and the second peak of high intensity at T = 467 K. These peaks coincide with the temperature recorded by DSC at 433 K and 462 K, respectively.

The significant evolution of the dielectric constant with diminishing frequencies is connected to the great contribution of the conductivity in this compound. The decrease of (ε') and (ε'') with rising frequency is linked to the large conductivity in our material owing to charge carriers and to the fast mobility of the proton H^+ [38,52].

The loss tangent $(\tan \delta)$, which is defined as the ratio of the loss factor (ε''_r) divided by the actual permittivity (ε'_r), is expressed as:

$$\tan \delta = \frac{\varepsilon_r''}{\varepsilon_r'}$$

Fig. 19 displays the fluctuation of the dissipation factor $(\tan\delta)$ as a function of temperature at different frequencies. It's clear that the dielectric loss exhibits similar values of the dissipation factor $(\tan \delta)$

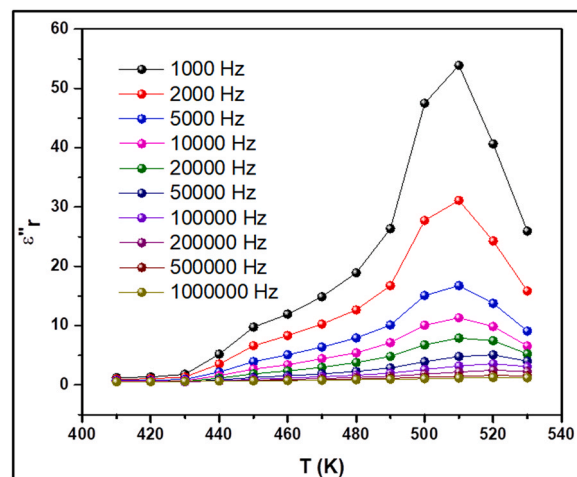
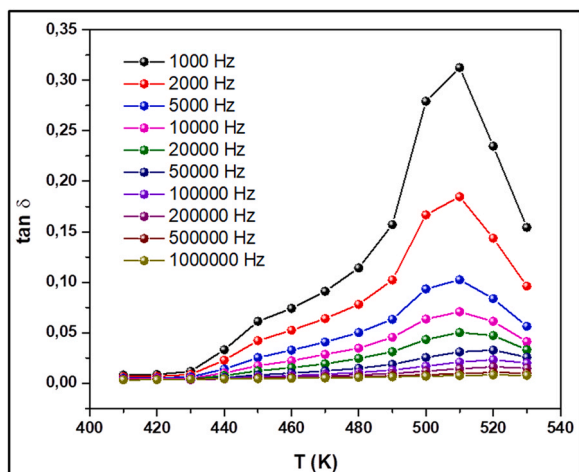**Fig. 18.** The temperature dependence of ε_r'' for C1.

Fig. 19. The temperature dependence of tan δ for C1.

with (ε'_r) and (ε''_r). The gotten values of the dissipation factor (tan δ) become higher with the important contribution of conductivity in the title material.

4. Conclusion

In summary, we synthesized a novel hybrid metal-halide material $(H_2Piper)_4[(FeF_6)_2FeF_5(H_2O)(H_2O)_4]$ by the hydrothermal method. The single X-ray diffraction crystal study reveals that this compound crystallizes in the triclinic system with P $\bar{1}$ space group. The structure of this material can be described as the recombination of two types of inorganic anions $[FeF_6]^{3-}$ and $[FeF_5(H_2O)]^{2-}$ separated by $[H_2Piper]^{2+}$ cations and free water molecules. The water molecules play a crucial role on the cohesion of the structure by means of hydrogen interactions. The stability of this structure is ensured by means of hydrogen interactions of type O–H⋯F and N–H⋯F interaction, creating the whole 3D network. The thermal studies of the title compound indicate the presence of two-phase transitions, which is corroborated by the electrical and dielectric analysis, as well as the decomposition of the sample at about 576 K. Complex impedance analysis over temperature and frequency allows the determination of the equivalent circuit and electrical measurements, and reveals that this material is a super protonic conductor. Additionally, the dependency of ac conductivity with frequency at different temperatures proves to obey Jonscher's universal power law. The variation of the exponent (s) as a function of frequency unveils that the correlated barrier hopping is (CBH) and (NSPT) model. The dielectric analysis indicates the presence of the dielectric relaxation phenomenon of this compound. At this stage of analysis, we could assert that our synthesis could be valuable in terms of opening further fruitful lines of investigation and offering pumicing future research direction. Indeed, it may serve as an enlightening guideline for a deeper and fuller investigation of this material.

Declaration of Competing Interest

The authors declare that they have no known competing financial interests or personal relationships that could have appeared to influence the work reported in this paper.

Acknowledgment

References

[1] S. Sivakumar, N.A. Mala, K.M. Batoo, M.F. Ijaz, Inorg. Chem. Commun. 134 (2021) 108959.
[2] N.A. Mala, S. Sivakumar, K.M. Batoo, M. Hadi, Inorg. Chem. Commun. 131 (2021) 108797.
[3] M.B. Brennan, S.G. Davies, J.A. Lee, A.L. Thompson, J.E. Thomson, J. Chem. Crystallogr. 45 (2015) 401.
[4] T. Dammak, M. Koubaa, K. Boukheddaden, H. Bougzhala, A. Mlayah, Y. Abid, J. Phys. Chem. C 113 (2009) 19305.
[5] Q. Sun, S. Liao, J. Yao, J. Wang, Q. Fang, Acta Crystallogr. Sect. E Struct. Rep. Online 68 (2012) 1317.
[6] T. Dammaka, S. Elleuch, H. Bougzhala, A. Mlayah, R. Chtourou, Y. Abid, J. Lumin, 129 (2009) 893.
[7] L. Dobrzycki, K. Woz´niak, J. Mol. Struct. 921 (2009) 18.
[8] D.B. Mitzi, K. Chondroudis, C.R. Kagan, IBM J. Res. Dev. 45 (2001) 29.
[9] C.R. Kagan, D.B. Mitzi, C.D. Dimitrakopoulos, Science 286 (5441) 945.
[10] A. Kessentini, M. Belhouchet, J.J. Suñol, Y. Abid, T. Mhiri, J. Mol. Struct. 1039 (2013) 207.
[11] K. Pradeesh, M. Agarwal, K.K. Rao, G. Vijaya Prakash, Solid State Sci. 12 (2010) 95.
[12] A. Vishwakarma, P. Ghalsasi, A. Navamoney, Y. Lan, A. Powell, Polyhedron 30 (2011) 1565.
[13] I. Abdi, K. Al-Sadhan, A. Ben Ali, Acta Crystallogr. Sect. E 70 (2014) 471.
[14] I. Abdi, K. Al-Sadhan, A. Ben Ali, Acta Crystallogr. Sect. E 70 (2014) 335.
[15] S. Hajlaoui, I. Chaabane, J. Lhoste, A. Bulou, K. Guidara, J. Alloy. Compd. 679 (2016) 302.
[16] M.S. Lassoued, A. Lassoued, M.S.M. Abdelbaky, S. Ammar, A. Gadri, A. Ben Salah, S. Garcia-Granda, J. Mater. Sci. - Mater. Electron. 29 (2018) 5413.
[17] B. Song, C. Qin, Y. Zhang, X. Wu, K. Shao, Z. Su, Dalton Trans. 44 (2015) 3954.
[18] F. Akrout, F. Hajlaoui, K. Karoui, N. Audebrand, T. Roisnel, J. Solid, State Chem. 287 (2020) 121338.
[19] L. Clark, L. Clark, M. Albino, V. Pimenta, J. Lhoste, C. Payen, J. Grenèche, V. Maisonneuve, P. Lightfoot, M. Leblanc, Philos. Trans. R. Soc. A 377 (2019).
[20] M. Era, S. Morimoto, T. Tsutsui, S. Saito, Appl. Phys. Lett. 65 (1994) 51.
[21] M. Smida, V. Pimenta, M. Leblanc, M. Dammak, V. Maisonneuve, Dalton Trans. 42 (2013) 15748.
[22] V. Murugesan, J.S. Cho, N. Govind, A. Andersen, M.J. Olszta, K.S. Han, G. Li, H. Lee, D.M. Reed, V.L. Sprenkle, S. Cho, S.K. Nune, D. Choi, A.C.S. Appl, Energy Mater. 2 (2019) 1832.
[23] S. Bouketaya, A. Elferjani, M.S.M. Abdelbaky, M. Dammak, J. Solid, State Chem. 277 (2019) 395.
[24] X. Li, J. Wang, Y. Zhao, X. Zhang, ACS Appl. Mater. Interfaces 10 (2018) 16901.
[25] I. Abdi, F. Alzahrany, J. Lhoste, J. Greneche, A. Ben Ali, J. Adv. Chem. 10 (2014) 2617.
[26] V. Pimenta, Q.H. Hanh Le, L. Clark, J. Lhoste, A. Hemon-Ribaud, M. Leblanc, J.M. Greneche, G. Dujardin, P. Lightfoot, V. Maisonneuve, Dalton Trans. 44 (2015) 17.
[27] M. Smida, J. Lhoste, M. Dammak, S. Garcia-Granda, Arab. J. Chem. 5 (2015) 2.
[28] S. Bouketaya, M. Smida, S.M. Abdelbaky, M. Dammak, S. García-Granda, J. Solid, State Chem. 262 (2018) 343.
[29] Y. Al-Douri, S.M. Hassan, K.M. Batoo, E.H. Raslan, Eur. Phys. J. 136 (2021) 295.
[30] L.J. Farrugia, WinGX and ORTEP for windows: an update, J. Appl. Cryst. 45 (2012) 849.
[31] G.M. Sheldrick, SHELXS-86: a program for structure solution, Gottingen Univ., Ger. (1986).
[32] G.M. Sheldrick, SHELXS-97: A Program for Crystal Structure, Gottingen University, Germany, 1997.
[33] O. Guesmi, M.S.M. Abdelbaky, D. Martínez-blanco, L. Ktari, S. García-Granda, M. Dammak, Inorg. Chim. Acta 496 (2019) 119033.
[34] S.B. Salah, P. Sidónio, F. Lefebvre, C. Ben Nasr, S. Ammar, M.L. Mrad, J. Mol. Struct. 1137 (2017) 553.
[35] W.H. Baur, Acta Cryst. 30 (1974) 1195.
[36] E.J. Walsh, J. Chem. Educ. 76 (1999) 95211.
[37] D. Abid, I. Dhouib, P. Guionneau, S. Pechev, I. Chaabane, N. Daro, Z. Elaoud, J. Alloy. Compd. (2020) 153826.
[38] A. Elferjani, S. Garcia-granda, M. Dammak, J. Alloy. Compd. 749 (2018) 448.
[39] K.M. Batoo, Alimuddin, S. Kumar, Int. J. Nanopart. 2 (2009) 416–422.
[40] K.M. Batoo, S. Kumar, C.G. Lee, Alimuddin, Curr. Appl. Phys. 9 (2009) 826–832.
[41] A.M.M. Farea, S. Kumar, K.M. Batoo, A. Yousef, C.G. Lee c, Alimuddin, J. Alloy. Compd. 464 (2008) 361–369.
[42] R.M. Hill, A.K. Jonscher, J. Non-Cryst. Solids 32 (1979) 53.
[43] H. Kchaou, K. Karoui, A. Ben Rhaiem, Physica E 85 (2017) 308.
[44] H. Kchaou, A. Ben Rhaiem, K. Karoui, F. jomni, K. Guidara, Appl. Phys. A 82 (2016) 122.
[45] S.R. Elliot, Adv. Phys. 36 (1987) 135.
[46] M. Ben Bechir, K. Karoui, M. Tabellout, K. Guidara, A. Ben Rhaiem, J. Alloy. Compd. 588 (2014) 551.
[47] A. Ghosh, Phys. Rev. B 41 (1990).
[48] P. Taylor, M. Pollak, Philos. Mag. (2011) 37.
[49] S. Mollah, K.K. Som, K. Bose, B.K. Chaudhuri, J. Appl. Phys. 74 (1993) 931.
[50] M. Megdiche, C. Perrin-pellegrino, M. Gargouri, J. Alloy. Compd. 584 (2014) 209.
[51] R. Ben Said, B. Louati, K. Guidara, J. Alloy. Compd. 672 (2016) 521.
[52] K.M. Batoo, S. Kumar, C.G. Lee, Alimuddin, Curr. Appl. Phys. 9 (2009) 1072–1078.